

**A comparison of OLR and circulation based indices for tracking
the MJO**

GEORGE N. KILADIS *

NOAA Earth System Research Laboratory, Physical Sciences Division, Boulder, Colorado

JULIANA DIAS

CIRES, University of Colorado and NOAA Earth System Research Laboratory, Boulder, Colorado

KATHERINE H. STRAUB

Department of Earth and Environmental Sciences, Susquehanna University, Selinsgrove, Pennsylvania

MATTHEW C. WHEELER

Centre for Australian Weather and Climate Research, Melbourne, Victoria, Australia

STEFAN N. TULICH

CIRES, University of Colorado and NOAA Earth System Research Laboratory, Boulder, Colorado

KAZUYOSHI KIKUCHI

International Pacific Research Center, University of Hawaii, Honolulu

KLAUS M. WEICKMANN

CIRES, University of Colorado and NOAA Earth System Research Laboratory, Boulder, Colorado

MICHAEL J. VENTRICE

WSI, 400 Minuteman Road, Andover, Massachusetts

ABSTRACT

Two univariate indices of the MJO based on outgoing longwave radiation (OLR) are developed to track the convective component of the MJO while taking into account the seasonal cycle. These are compared with the All Season Real-Time Multivariate MJO (RMM) Index of Wheeler and Hendon derived from a multivariate EOF of circulation and OLR. The gross features of the OLR and circulation of composite MJOs are similar regardless of the index, although RMM is characterized by stronger circulation. Diversity in the amplitude and phase of individual MJO events between the indices is much more evident; this is demonstrated using examples from the Dynamics of the MJO (DYNAMO) field campaign and the Year of Tropical Convection (YOTC) virtual campaign. The use of different indices can lead to quite disparate conclusions concerning MJO timing and strength, and even as to whether or not an MJO has occurred. A disadvantage of using daily OLR as an EOF basis is that it is a much noisier field than the large-scale circulation, and filtering is necessary to obtain stable results through the annual cycle. While a drawback of filtering is that it cannot be done in real time, a reasonable approximation to the original fully filtered index can be obtained by following an endpoint smoothing method. When the convective signal is of primary interest, we advocate the use of satellite-based metrics for retrospective analysis of the MJO for individual cases, as well as for the analysis of model skill in initiating and evolving the MJO.

**Corresponding author address:* George N. Kiladis, Physical Sciences Division, ESRL, 325 Broadway St., Boulder, CO 80305-3328.

E-mail: george.kiladis@noaa.gov

1. Introduction

The MJO needs little introduction. Since its discovery more than 40 years ago (Madden and Julian 1971, 1972), hundreds of studies have addressed its observed structure, the theoretical basis for its existence and behavior, and the ability of models to simulate and forecast this critically important phenomenon. Detailed reviews of the MJO can be found in Zhang (2005), Wang (2006), and Lau and Waliser (2011). Although much progress has been made in understanding and forecasting the MJO over the past four decades, it remains a significant outstanding problem in tropical meteorology (see Zhang et al. 2013).

As discussed in detail by Straub (2013) (hereafter S13), one of the challenges faced by researchers studying the MJO has to do not only with tracking the disturbance through time, but simply defining it. This difficulty stems from the fact that the MJO is associated with strong planetary circulation anomalies, and similar circulations are at times not accompanied by an organized convective signal (Weickmann and Berry 2009). In addition, when present, the convective signal is not a discrete entity, but rather appears in satellite imagery as planetary-scale “envelope” of intermittent higher-frequency convective activity that is not necessarily systematically organized (Dias et al. 2013). It is also well known that the location and behavior of MJO convection is strongly dependent on the seasonal cycle, enough so that during the Asian monsoon rainy season, it is often referred to as the “Boreal Summer Intraseasonal Oscillation” (BSISO) or simply the “ISO” (Waliser et al. 2012; Kikuchi et al. 2012; Lee et al. 2013; DeMott et al. 2013).

Many approaches have been designed to identify the MJO in observations and numerical simulations. This wide variety of definitions has led to an effort to standardize these metrics in order to provide “apples to apples” comparisons, particularly of model output (Sperber and Waliser 2008; Gottschalck et al. 2010).

Wheeler and Hendon (2004) (WH04) developed the Real-Time Multivariate MJO (RMM) index to calculate the state of the MJO utilizing latitudinal averages of OLR and the zonal wind at 200 and 850 hPa. This particular index has become standard for monitoring the state

of the MJO in real time and in models (Lin et al. 2009; Gottschalck et al. 2010; Rashid et al. 2011; Hamill and Kiladis 2013). RMM has also been used in many statistical studies of both the structure of the MJO and its impacts on tropical cyclones (Klotzbach 2010; Belanger et al. 2010; Ventrice et al. 2011), remote circulation and storm track changes (Moore et al. 2010), and even U.S. tornado outbreaks (Thompson and Roundy 2013). An advantage of the RMM is that the large-scale circulation data smooths the signal so that pre-filtering is unnecessary except to remove the seasonal cycle and interannual variability, which can be conveniently performed in real time by subtracting out the previous 120-day running average. A recently derived variant of the RMM replaces input from OLR with 200-hPa velocity potential (Ventrice et al. 2013), which has long been used to track the MJO (Lorenc 1984). This VP-MJO index (VPM, see: <http://www.esrl.noaa.gov/psd/mjo/mjoindex/>) appears to better discriminate the MJO signal during boreal summer, and improves the relationship of the MJO with Atlantic tropical cyclone activity.

As documented by S13, the fact that the RMM amplitude may at times be weak even with the presence of an “MJO-like” convective signal, or strong in the absence of such a signal, raises the question of which fundamental characteristics of the MJO should be used to define it. While we will not directly address this issue here, we point out that the essential circulation features of MJO teleconnections in both the tropics and extratropics can be reproduced in a dry primitive equation model by forcing associated with its diabatic heating field (Matthews et al. 2004; Seo and Song 2012). With this in mind, our goal is to suggest alternate approaches that more closely track the location of the MJO convective signal and can be used throughout the seasonal cycle. Despite the large diversity of disturbances comprising individual MJO events, spatial-temporal EOF analysis of satellite-derived cloudiness data lends itself well to this purpose (Lau and Chan 1988; Zhang and Hendon 1997; Kikuchi and Takayabu 2003; Sperber 2003). For appropriately filtered satellite irradiance data, two leading eigenvectors derived from their associated covariance matrix can be combined to construct an index to describe both the amplitude and phase of the disturbance. Less compact

indices involving higher mode EOFs (Roundy and Schreck 2009) are also useful for tracking relationships between the MJO and other convectively coupled equatorial waves Wheeler and Kiladis (1999) (hereafter WK99) (Kiladis et al. 2009), but due to their simplicity and convenience two mode indices are by far most often used.

A practical two mode MJO index can be obtained by using OLR data throughout the year (e.g. Slingo et al. 1999; Matthews 2008); however, the spatial patterns of the resulting EOFs tend to be concentrated close to the equator and do not represent the seasonal latitudinal migration of the MJO. To get around this problem, EOFs have been calculated separately for different times of the year (Waliser et al. 2003; Kikuchi et al. 2012), or latitudinally averaged OLR data has been used as the EOF basis, while choosing a range in latitude such as 15°S-15°N that spans the full seasonal migration of the MJO (Maloney and Hartmann 1998; Kessler 2001). However, EOFs derived in this way can also misrepresent the amplitude of the OLR signal due to the potential for cancellation of opposite signed anomalies in the latitudinal averaging (e.g. Ventrice et al. 2011).

This paper extends the work of Kikuchi et al. (2012), who developed two separate OLR extended EOFs for boreal summer and winter, by essentially “filling in” the intervening seasons with a smoothly varying OLR EOF analysis. In Section 2, this and an alternate OLR MJO index are developed. In Section 3 these indices are statistically compared with the RMM for two different periods with large amplitude MJO activity. Section 4 examines MJO initiation using a methodology similar to S13, and in Section 5 a method derived by Kikuchi et al. (2012) to adapt filtered time series for real time monitoring is applied to the derived indices. This is followed by a discussion and conclusions in Section 6.

2. Data and Methodology

The calculation of an all-season OLR-based MJO Index (OMI) is a straightforward application of an EOF analysis of spatially gridded OLR. In this study, we utilize the standard

daily 2.5° resolution OLR dataset that has been interpolated in time and space to replace missing values (Liebmann and Smith 1996). EOFs are derived using the period 1979-2012, and circulation associated with the OMI and RMM is derived from ERA Interim reanalysis products (Dee et al. 2011).

a. Derivation of OMI

The first step in deriving the OMI is to filter OLR to retain only frequencies associated with the MJO. Filtered OLR between 20°S-20°N is then subjected to a standard covariance matrix EOF analysis that retains the local variance of the OLR fluctuations. All tests were conducted using a 96-day period at the low frequency end of the band to remove interannual variability, following WK99.

We initially tested EOF results using 20-day high frequency cutoff, which is often used to capture more rapid evolution and reorganization of MJO convection (e.g. Matthews 2008; Ling et al. 2013). This was motivated by the fact that the MJO does not always propagate steadily eastward, but appears at times to reorganize to the west, often due to interactions with equatorial Rossby (ER) waves (Roundy and Frank 2004; Masunaga 2007; Gloeckler and Roundy 2013). As recently shown by Zhao and Zhou (2013), 20-96 day bandpass filtered data yields a usable index when centered on boreal winter, but this approach resulted in either a pair or three degenerate modes not separable by the criterion of North et al. (1982) for the rest of the year. Similar problems were encountered using 20-96 day eastward-only filtered data, and truncating to retain only the lowest wavenumbers was also not effective. After extensive testing it was evident that 30-96 day eastward-only filtered data (including the zonal mean and all wave numbers) gave the most stable results for all seasons. This is similar to the “MJO-band” as originally used by WK99, except that only eastward waves 0-5 were retained in that study. While there is little difference in the results for large-scale fields, retaining higher wavenumbers results in more detailed derived spatial eigenvector fields.

Since the MJO displays a significant seasonal shift in its location, especially in convection

(WK99), it is important to apply the EOF analysis to a sufficiently short portion of the seasonal cycle, especially during the transition seasons. To accomplish this, we calculated EOFs using all years from 1979-2012 but centered on each day of the calendar year using a sliding window. As might be expected, eigenvector pairs for adjacent days were nearly identical, once arbitrary sign reversals are accounted for.

Results were initially tested for various time window lengths ranging from 31 to 121 days. In all cases the two leading EOFs explain nearly the same amount of variance and represent a propagating pair. Experimentation found that a window length of 121 days was optimal, as it retains good resolution of the seasonal variability yet minimizes the problem of the EOFs becoming degenerate except during one period late in the year (discussed below). The percentage of variance explained is remarkably stable across window lengths and seasons, and the leading EOFs are also well separated from the third EOF, which generally explains less than 5% of the variance compared with more than 26% each for EOFs 1 and 2.

Figure 1 shows the eigenvalues for EOF1 and EOF2 for each day of the year derived using 30-96 day eastward OLR and a sliding 121-day window. These track each other well, differing by only 1-2% throughout, and peak during mid-January at greater than 65% of the total variance. The combined explained variance is minimized in late October, but is still above 53%. For a few days in early November the EOFs become degenerate, resulting in a mixing of the eigenvector structures and significant changes in those structures from one day to the next. Since it was difficult to cleanly separate the EOFs during this period, the patterns from November 1 and November 8 were linearly interpolated to fill in the intervening days to obtain a smoothly varying index over that period. The resulting 365 pairs of spatial EOFs effectively represent the propagation of the MJO convective envelope throughout the year by smoothly filling in the equinoctial transition seasons between the two EOF pairs isolated by Kikuchi et al. (2012) centered on the solstice seasons.

Examples of the OLR EOF spatial patterns for January 15 and July 15 are shown in Fig. 2. The January 15 patterns are very similar to those obtained by the studies referenced

in Section 1, which used similar approaches to categorize the boreal winter MJO, with the EOF pair and its inverse together representing an eastward propagation of dipole convective anomalies from the Indian sector to the western Pacific. The July 15 pair by contrast represents the propagation of convection from the equatorial Indian Ocean both poleward and eastward over southern Asia characteristic of the boreal summer MJO.

While the PC pairs do represent the location of the MJO-filtered OLR data from which it was derived, the varying strength of the MJO at sub-intraseasonal scales is not well represented due to the filtering used to derive the index (not shown). However, it is still possible to account for the higher frequency behavior of the MJO by projecting less filtered OLR data onto the derived spatial EOFs. For this purpose, we used 20-96 day filtered OLR data, and also include all eastward and westward propagating zonal wavenumbers (to zonal wavenumber 72). Note that the resulting phase and amplitude information is not the same as an EOF analysis of 20-96 day filtered data discussed above, which did not yield two consistent EOFs through the seasonal cycle; nevertheless, a comparison with the 20-96 day EOFs during DJF when the results are stable shows a close correspondence. Further experimentation suggests that the 20-96 day filtered data still represents the large-scale behavior of the MJO in OLR while avoiding excessive noisiness in the index, and also better accounts for the timing of changes in the OLR field related to the sometimes rapid reorganization of the convective field.

Once the 20-96 day filtered OLR for each day in the 1979-2012 record has been projected onto the corresponding spatial EOFs associated with that day of the year, the PCs are normalized. Since the spatial variance of each eigenvector is equally weighted, we normalize OMI PC1 to have a standard deviation of 1, and the same scaling is used to normalize PC2 to retain its relative weighting with respect to PC1. The resulting standard deviation of PC2 is .90. The corresponding spatial EOF patterns are then rescaled so that the original fields can be reconstructed for any given day using:

$$\hat{Y}(t) = EOF1_j \times PC1(t) + EOF2_j \times PC2(t) \quad (1)$$

where the subscript j refers to the EOF spatial pattern for the corresponding day of the year, and t refers to the date. It is important to note that the scaling of the OMI differs from that of the RMM, where both PCs are normalized to unit variance. For RMM reconstruction, the corresponding spatial EOF structures are instead scaled by a normalization factor and their respective eigenvalues (see <http://cawcr.gov.au/staff/mwheeler/maproom/RMM/index.htm>).

The normalized OMI PCs comprise an OLR-only based two-component index of the MJO, so the two PCs can be plotted on a phase diagram in an analogous manner to the RMM index. Finally, it turns out that the indices for any date throughout the year are directly comparable between the RMM and OMI when the sign of OMI PC1 is reversed and the PC ordering is switched, so that OMI(PC2) is analogous to RMM(PC1) and $-$ OMI(PC1) is analogous to RMM(PC2). We use these adjusted OMI PC phase and sign conventions here so that they can be directly compared with those of the RMM. A summary of these and other indices considered below, with a short description of their derivation, is given in Table 1.

The bivariate correlation is one method of measuring the linear relationship between PC pairs (Gottschalk et al. 2010), and these have been calculated for all combinations of indices in this study (Table 2). The maximum bivariate correlation is .70 for daily values of OMI and RMM using the entire record, ranging from .79 during MAM to .63 in JJA. Table 2 also reveals that on average the temporal phasing between OMI and RMM is within a day during DJF and MAM, but that this is displaced by up to four days during SON. Differences in phasing are to be expected due to the imprint of circulation on the RMM, and it is important to adjust for these when comparing indices.

b. An alternate Filtered MJO OLR (FMO) index

The OMI provides a way to categorize the large-scale cloudiness field of the MJO with a bivariate index like the RMM. A drawback, however, is that it requires the use of individual daily EOF patterns in order to reconstruct the two-dimensional MJO OLR field for a given

208 day using eq. (1). Another potential inconvenience of the OMI involves the effort needed to
 209 calculate running EOFs for model output. It would therefore be desirable to use an “RMM-
 210 like” methodology to derive a year-round OLR-only index that does not rely on circulation
 211 input. As shown above and also by WH04 and S13, using daily OLR anomalies for such
 212 an approach is unacceptably noisy. However, using filtered OLR as input to the RMM
 213 methodology yields more reasonable results.

214 One option is to simply project filtered daily OLR onto the original RMM OLR EOFs,
 215 and this turns out to be a useful index in itself. However, a somewhat better alternative is to
 216 derive the univariate OLR EOFs directly from 20-96 day filtered OLR (using all wavenum-
 217 bers) averaged between 15°S-15°N using the same procedure as described by WH04 for the
 218 full RMM. Although these spatial EOFs look similar to the OLR eigenfunctions of WH04
 219 (not shown), differences in phasing and amplitude are important for the correct timing of
 220 MJO initiation, as described below. As with OMI we do not normalize the PCs to one, but
 221 instead retain the relative weights with respect to equally weighted spatial EOFs. This is also
 222 important for maintaining the correct phase and amplitude of the index, since even though
 223 the RMM PCs both have equal variance, the associated OLR spatial EOFs are not weighted
 224 in the same way as a univariate OLR would be since the multivariate analysis includes wind
 225 components. After reversing the order of the PCs, the resulting Filtered MJO OLR (FMO)
 226 index has the same phase convention as RMM. The bivariate correlation between the PCs
 227 for the OMI and FMO for the entire 1979-2012 period is .90, with the largest correlations
 228 at zero lag (Table 2), ranging from .95 during DJF to .83 during JJA. We note that while
 229 the alternate index obtained by projecting 20-96 day filtered OLR onto the original RMM
 230 OLR EOFs has a bivariate correlation with FMO of .96, their phases are less well correlated
 231 (.79).

3. Comparison of indices

a. Statistical Comparison

It is of interest to compare the OMI spatial EOF patterns with the corresponding patterns of the leading two modes for the RMM index. Since the RMM EOFs involve latitudinally averaged fields, we reconstruct their two-dimensional spatial patterns for a specific time of the year by projecting a given field onto the PC time series through linear regression. This approach yields less noisy fields than phase space composites, although it is still problematic to scale them consistently due to their amplitude and phasing differences, which vary substantially throughout the year, so such a comparison is necessarily qualitative.

Figure 3 shows the projections of the unfiltered OLR and 850 hPa streamfunction fields onto the two RMM and OMI PCs for December-February (DJF), and in Fig. 4 the 200 hPa streamfunction and OLR for June-August (JJA). These fields are scaled by two standard deviations of their respective PCs, a departure representative of a typical strong MJO event. FMO fields (not shown) are nearly identical to those using OMI.

As expected, the OMI OLR patterns in Figs. 3c,d and 4c,d are very similar to those in Fig. 2 within the 20°S-20°N domain. The OLR fields for RMM also strongly resemble those for OMI, as well as the large-scale features of the circulation, indicating that gross statistical relationships derived using the RMM index are indeed similar to what might be derived from an OLR-only index. However close inspection reveals some less subtle differences. For example, substantial contrasts in the 850 hPa streamfunction are seen between Figs. 3b and 3d, with RMM showing a cyclone which is stronger by a factor of two over the north Pacific displaced to the southeast of the corresponding feature in Fig. 3a, and overall stronger circulations in both hemispheres. Other contrasts exist within the panels of Figs. 3 and 4, with stronger RMM circulations despite comparable OLR fields. These differences persist even after adjusting for the 1-2 day lag shown in Table 2 between the indices and the root-mean square differences in the amplitudes of OLR fields, confirming that even for a very

similar diabatic heating field distribution, the resulting RMM circulation is substantially impacted in both the tropics and extratropics by the use of the tropical zonal wind in deriving the index.

Although the regressed representation of the MJO is to some level of detail similar between the OMI and RMM, composites based on individual index phases reveal much larger differences (these are available at: <http://www.esrl.noaa.gov/psd/mjo/mjoindex/> which also stores the spatial patterns and the associated retrospective and real time PCs for the OMI and FMO). In general, the use of OLR as an EOF basis results in much larger OLR perturbations for OMI composites in all phases, and consequently substantial circulation contrasts even within the tropics. As we will demonstrate, for individual cases there are also large differences between the indices, as was shown by S13 for alternate forms of the RMM itself.

b. Examples from the DYNAMO period

The Dynamics of the MJO (DYNAMO) field experiment was designed to enhance the knowledge and forecast skill of MJO initiation and evolution over the Indian Ocean (Zhang et al. 2013). Several “MJO-like” events took place during DYNAMO, each with their own distinctive attributes (Gottschalck et al. 2013; hereafter G13; Yoneyama et al. 2013; hereafter Y13; Johnson and Ciesielski 2013; hereafter J13). The OLR anomaly field averaged from 10°S-10°N during the October 2011 through March 2012 DYNAMO period is shown in Fig. 5, along with contours of MJO-filtered OLR (WK99). The anomaly was calculated by removing the first three harmonics of the mean seasonal cycle, and so retains interannual variability.

Eastward propagation of primarily negative OLR perturbations is dominant during DYNAMO, with two well-defined MJO events during October (MJO1) and November (MJO2; Y13, J13). Two pulses of westward propagation starting from around 140E are evident in mid- and late December, followed by a re-establishment of a convective signal over the western Indian Ocean in mid-January. The first event culminated in a strong projection

284 onto an ER mode in the central Indian Ocean in late December (G13), and despite the
 285 eastward propagation seen in Fig. 5 the late December event only weakly projects onto the
 286 MJO filtered band, although this is referred to as MJO3 by Y13 and a “mini-MJO” by G13,
 287 reflecting its smaller scale and relatively fast propagation speed.

288 These events were followed by eastward-propagating convective activity originating over
 289 the Indian Ocean from mid-January to early February, superimposed on three westward
 290 propagating features that map onto ER waves (G13). This event does have a weak MJO-
 291 filtered OLR signal, although its apparent eastward propagation in Fig. 5 is influenced by
 292 the development of three tropical disturbances over the Australian monsoon region at this
 293 time. The DYNAMO period culminates in the unusually large amplitude “MJO4” during
 294 March 2012. Further details of the convective evolution during DYNAMO can be found in
 295 G13, Y13 and J13.

296 In Fig. 6 the phase diagrams for RMM, OMI, and FMO are shown for the period October
 297 2011 through March 2012. Phase diagrams of circulation-only RMM (S13) and the Ventrice
 298 et al. (2013) VPM index described above are not shown here since they correlate so highly
 299 (.90 and .91, respectively) with RMM.

300 The dominance of MJO activity in the OLR field of Fig. 5 is reflected in the behavior
 301 of the indices in Fig. 6. Sustained amplitude outside the unit circle is often utilized to
 302 determine whether MJO activity is occurring (S13), and the RMM (Fig. 6a) shows ampli-
 303 tudes exceeding 1.0 throughout most of the 6-month period, along with nearly continuous
 304 eastward (counterclockwise) propagation. The more smoothly propagating OMI and FMO
 305 also display nearly continuous large amplitudes, with the notable exceptions of the October
 306 and December periods.

307 While the RMM index does track the evolution of many of the main convective features
 308 during DYNAMO, Fig. 6a gives the impression that the MJO was most active during mid-
 309 October. The RMM amplitude reaches a peak of 3.6 in sector 1 during MJO1, then rapidly
 310 decreases in late October at a time when convection is actually developing and shifting

eastward over the Indian Ocean in Fig. 5. By contrast, the OMI amplitude is less than 1.0 until October 17, when it rapidly increases in response to the onset of convection over the Indian sector seen in Fig. 5. The OMI amplitude reaches a much smaller maximum (1.35) than RMM on October 25, matching the timing of the peak of convection during MJO1. Thus the OMI better captures the onset and evolution of MJO convection in the Indian sector in this case, with the large loading onto RMM during mid-October attributed almost entirely to the circulation component.

As expected, the FMO tracks OMI much more closely than RMM. For example, the amplitude in sectors 7 through 1 of the October event are downplayed when compared to the RMM, and if we assume that “initiation” occurs when the index becomes greater than 1.0 (S13), the timing of MJO1 initiation and peak convection is similar but a bit more than one sector farther west for than the OMI. In this case, the FMO is influenced by both the convectively coupled Kelvin wave pulses over Africa seen in Fig. 5, and the cancellation of the OLR signal due to latitudinal averaging (not shown), neither of which strongly affect the OMI.

All indices show similar behavior through November, progressing through the Maritime Continent and Western Hemisphere with a full rotation from sector 4 back to sector 3 associated with the suppressed MJO signal and the initiation of the successive MJO2 event over the Indian Ocean. As MJO2 initiates over the western Indian sector around November 20 and moves eastward, it becomes smaller in scale and rapidly progresses to the Maritime Continent. The latter stages of this event map onto the convectively coupled Kelvin wave (G13), and despite this transition the RMM maintains its relatively high amplitude through December 10, whereas OMI and FMO both rapidly decay to within the unit circle by the first of the month.

The westward propagation of convection discussed above during mid-December is represented in all three indices by a small loop and interruption of counterclockwise progression from sector 4 to 6, most prominent in the FMO. Once eastward propagation resumes on De-

338 cember 20, the OMI and FMO decay rapidly to below amplitude 1.0, and reemerge in sector
 339 7 with the development of the suppressed phase around January 1. Therefore this event
 340 would not be considered an MJO by the use of these metrics. This is also reflected by the
 341 weakness of the MJO-filtered OLR signal in Fig. 5, even though there is nearly continuous
 342 RMM loading of above one during the same period, also noted by G13 and Y13. As pointed
 343 out in these studies, this event was MJO-like with respects to dynamics and even in OLR
 344 depending on the filtering used, emphasizing the need to consider a variety of diagnostics
 345 when characterizing individual events.

346 The indices are in reasonably good agreement on the timing of the rapid eastward prop-
 347 agating OLR signal in late January-early February, although as noted above this feature
 348 does appear to be strongly influenced by tropical storm development over Australia and its
 349 categorization as an MJO is doubtful. The behavior of the indices leading up to this period
 350 illustrates their potential pitfalls. The appearance of a suppressed MJO filtered OLR en-
 351 velopes in Fig. 5 during early January leads to a relatively large amplitude counterclockwise
 352 signal in Figs. 6d and 6f in OMI and FMO when compared to lower amplitude RMM in
 353 Fig. 6b. Then starting in late January larger amplitude counterclockwise rotation is seen
 354 into February in all three indices. The loading onto RMM is due almost entirely to the
 355 circulation component (not shown), whereas in the case of OMI and FMO it results from
 356 the two suppressed MJO filtered OLR envelopes during January and February in Fig. 5,
 357 which are present despite the lack of accompanying coherent eastward propagating signals
 358 in the unfiltered fields. This is likely due in part due to the spectral ringing effects of the
 359 intraseasonal filtering with the imprint of the large amplitude March MJO4 event extend-
 360 ing back in time. In all cases these signals would lead to the classification of MJO4 as a
 361 successive event, also inferring that late January event should be classified as an MJO. The
 362 indices all capture the timing of the onset of MJO4 Indian Ocean convection at the end of
 363 February, and although there are some differences in amplitude and phasing, that event is
 364 represented with appropriately large amplitudes.

c. Examples from the YOTC study period

To provide a comparison with the DYNAMO period, we consider the MJO activity during the Year of Tropical Convection (YOTC: Moncrieff et al. 2012; Waliser et al. 2012) virtual experiment. As with DYNAMO, much of the YOTC study effort is devoted to verification of models abilities to simulate the MJO (Zhang et al. 2013), and so the fidelity of the metrics that are used to assess the integrity of the MJO within these simulations are of particular interest. Fig. 7 shows the 10°S-10°N OLR anomaly and MJO-filtered OLR for the period October 2009 through March 2010. This period was chosen for study during YOTC because a well-defined MJO occurred during late October-November followed by another stronger event from late December into February.

The RMM, OMI, and FMO phase diagrams for YOTC are shown in Fig. 8. All show an MJO initiation occurring within a couple of days of October 25, but FMO and especially OMI better capture the amplification of the convective signal over Indian Ocean sectors 2 and 3 seen in Fig. 7. The indices then all similarly track the MJO to the Maritime Continent sectors, followed by a roughly similar evolution of the November suppressed event, except for the fact that RMM leads OMI by more than one sector with FMO phasing lying in between. This lag is partly consistent with the bivariate correlations between the two indices during SON as shown in Table 2, where the OMI (FMO) is seen to lead the RMM on average by 4 (2) days.

A larger contrast is seen in the treatment of the second MJO. This event starts farther east than the first MJO around mid-December (Fig. 7), and the OMI and FMO capture this amplification just after December 20 in the eastern Indian Ocean (sector 3) when the RMM still shows large amplitudes over the Western Hemisphere. The RMM phase catches up to OMI and FMO by early January (Fig. 8a); however, the RMM remains at a relatively low amplitude even with the strong convection that develops over the western Pacific, with the OMI and FMO at more than double the RMM values in sector 6 around mid-month. By mid-February, large phase lags are again evident with the OMI and FMO both responding

to the suppressed region of convection over the Maritime Continent with large loadings in sectors 8 through 2. By late February all indices are back within the unit circle, with the OMI and FMO both remaining low amplitude until the end of the period. RMM, however, then amplifies into March, suggesting MJO initiation over the Indian Ocean and progressing to the Maritime Continent, despite the overall lack of convection seen then in Fig. 7.

In summary, the OMI appears to be successful in capturing the convective component of the MJO, and a useful bivariate FMO index can be obtained relatively easily using appropriately filtered OLR data. Although the FMO only provides direct information on the latitudinally averaged OLR field, it is easily derived and, like RMM, provides one EOF pair to represent the state of the convective field of the MJO throughout the entire year, with the caveat that its amplitude and phase may not be fully representative of the large-scale convective field. We have not shown the corresponding phase diagrams for the alternate index obtained by projecting 20-96 day OLR data onto the original WH04 OLR EOFs, but this may be another useful option since it displays similar behavior to the FMO, although the FMO better preserves phase and amplitude information with respect to the OMI.

4. MJO Primary Initiation in RMM, OMI and FMO

A potentially very useful application of an index such as RMM and OMI is that their PC amplitudes can be used to determine “MJO initiation” over a certain sector. However, as discussed in detail by S13, such a determination necessarily involves subjective decisions as to what comprises an MJO event, including choices about the amplitude threshold and length of time that it must remain above this value. Here we briefly examine the robustness of primary MJO events, that is, those that originate without any immediate precursor MJO (Matthews 2008), in RMM, OMI, and FMO using a range of simple criteria.

The sensitivity of OMI and RMM primary initiation events was determined by testing various parameters similar to those used by S13. The initiation of an MJO was defined as the

date when the index crossed a given threshold value, after remaining less than that value for a certain number of days, and then exhibiting counterclockwise rotation on the phase diagram for a set number of days. Three amplitude thresholds of 1.0, 1.1 and 1.2 were used, and the required number of days for an amplitude of less than the threshold prior to initiation ranged from 7 to 9, while the number of days of counterclockwise rotation was varied from 3 to 7. Counterclockwise rotation was defined based on the first and last day of amplitude greater than the threshold rather than requiring continuous rotation, which would have eliminated many of the RMM events due to day-to-day noise. These less stringent criteria yielded many more RMM primary events than obtained by S13 (their Table 2).

Figure 9 shows the results of these tests in histogram form, which gives the number of initiation events by sector depending on the parameters chosen. While it is difficult to completely convey all details of these results in one figure, several features of this plot are immediately obvious. First, the number of initiations varies greatly depending on the criteria used for all three indices, but in general the use of OMI and FMO results in substantially more events due to the noisiness of the RMM. RMM initiations are more evenly distributed among the sectors, with FMO and OMI initiation tending to favor sectors 2 and 6 for all parameter combinations. This results from OMI and FMO EOFs favoring the sectors where loading onto the OLR spatial EOFs is the greatest (Fig. 2). Sector 2 corresponds to the most common initiation location of the MJO convective signal over the central Indian Ocean, and the peak over sector 6 reflects both the tendency for suppressed MJO phases to start over the Indian Ocean, as well as a secondary peak in MJO convective initiation over the west Pacific warm pool. Likewise, local minima in sectors 4, 7, and 8, indicate a reduced likelihood of initiation over the Maritime Continent and Western Hemisphere.

For primary events as defined here, the statistics on MJO convective initiation over the range of global sectors using OMI and FMO appear to be in line with what would be expected from their corresponding EOF spatial patterns, and they are much more robust regarding the date of initiation to changes in criteria than is the RMM. To illustrate the latter point,

Table 3 shows the percentage of primary initiation dates that match, for each individual index, to within ± 3 days obtained by varying the range of parameters used to produce Fig. 9. Percentages are shown for three amplitude thresholds: 1.0, 1.1, and 1.2. For the frequently used threshold of 1.0 used to define MJO activity, only 23% of the RMM dates match the other RMM dates, with more than double that (55% and 51%) for OMI and FMO, respectively. These numbers change little as the overlap window is extended. Statistics on the mean number of overlapping primary events between RMM, OMI, and FMO for the various criteria used in Figure 9 and Table 3 are also revealing. Table 4 shows that, when averaged over all threshold ranges, fewer than 15% of RMM primary initiation days overlap with OMI and FMO for windows ranging from 3 to 7 days. Even though the overlap between OMI and FMO is better, it is still just 37% for ± 7 days, and improves to only 42% for ± 14 days.

Attempts to classify successive MJO events using criteria similar to those used by S13 led to widely varying distributions in all indices, to the extent that it was difficult to achieve stable results for any reasonable range of parameters. Overall, although OLR-based indices do show more consistency for events that have no immediate precursor over a given sector, the results of this section illustrate the difficulties in objectively defining MJO initiation. Thus approaches such as those used by Ling et al. (2013) must be used, where for example amplification of OLR or precipitation anomalies over the Indian Ocean are categorized by physically based but still subjective criteria.

5. Real-Time Applications for MJO Monitoring and Modeling

Even though calculating the OMI and FMO require filtering, Kikuchi et al. (2012) showed that approximations of similar indices could be obtained in real time by smoothing OLR time series near the endpoints and then projecting these data onto the spatial EOFs of the index.

Here, we examine an application of this technique using OMI and FMO.

Following Kikuchi et al. (2012), we derive a real time OMI (ROMI) from OLR anomalies (with the mean and first three harmonics of the seasonal cycle removed) by first subtracting out the mean of the 40 days prior to the endpoint (or “target”) date to remove low frequency variability. We then apply a 9-day running average, tapered to use only the remaining days as the target date is approached, to remove intraseasonal variability. The resulting OLR values are then projected onto the OMI spatial EOF pattern corresponding to the target date. Here the number of prior and running average days was determined by optimizing the correlation of the PCs with those of the observed OMI for the entire retrospective period (1979-2012), and these turn out to be nearly identical to values obtained by Kikuchi et al. (2012) for their real time Extended EOFs (40 and 5 days, respectively). The bivariate correlation between the ROMI and the OMI is .90 when OMI leads by 2 days. The corresponding real time FMO (RFMO) was also calculated in the same manner, except that the 15°S-15°N averaged running OLR values were projected onto the FMO spatial EOF pair. The RFMO correlates at .86 with FMO at a one day lead, so this procedure works slightly better for OMI.

Figures 10a,b show the time series of the normalized ROMI and RFMO versus the OMI and FMO for the October-March DYNAMO period. Both real-time renditions track the fully filtered counterparts of their indices well, and, although noisier, the phase diagrams for ROMI in Figs. 10c, d show a reasonable correspondence to their corresponding OMI plots in Figs. 6c, d. For example, ROMI reflects the timing and phasing of MJO1 amplification in the proper Indian Ocean sector, although the timing of its crossing of the unit circle precedes that in the OMI plot by five days. ROMI deemphasizes the November and January suppressed phases over OMI, but this is not unreasonable given the weakness of the associated OLR anomalies in Fig. 5. Several other periods inspected (including YOTC) also show results that would be quite useful in a real-time setting, especially once the phasing differences between OMI and ROMI are accounted for by the mean offset of 2 days.

These results demonstrate that the temporal filtering to derive an index does not neces-

sarily preclude its use for real time monitoring. Since any time series can be projected onto a derived spatial EOF pattern, for example when daily data is used, the reduction of noise can be optimized with appropriate one-sided filtering when tuned to a fully filtered PC time series. A similar procedure can also be employed for model output where OLR or precipitation from short period runs used in forecast experiments would also require smoothing. As was pointed out by Kikuchi et al. (2012), it is likely that the smoothing algorithm utilized here could be improved upon by using more sophisticated techniques for one-sided filtering, as described for example by Arguez et al. (2008). Such an approach may even be useful for the development of alternative retrospective MJO metrics, since spectral ringing effects would be reduced by not using future data in the calculation of filtered indices. We plan to pursue such an approach in future work.

6. Discussion and Conclusions

As discussed in detail by S13 and Ling et al. (2013), objectively identifying individual MJO events and their initiation is problematic. This is despite the fact that even for MJO indices that are comprised of differing parameters, very similar results are obtained for the gross statistical features of the MJO, as has been demonstrated in many past studies and in Section 2 for RMM and OMI. The existence of so many different indices utilized to study the MJO illustrates its robustness, but also reflects the reality that no one index will suffice for every application. Because of its many advantages, the RMM has been widely used to study and monitor the MJO, however it is important to be aware of its limitations, as well as those of other MJO metrics that have been developed over the years.

Indices that use latitudinally averaged fields as a basis do not necessarily represent the boreal summer MJO as well (Ventrice et al. 2011; Lee et al. 2013); this is especially true for univariate OLR EOFs where there is often large meridional cancellation (see Figs. 2 and 4). In addition, the RMM is susceptible to influence by other convectively coupled waves

(Roundy et al. 2009), so it is desirable to filter for intraseasonal time scales as a first step in deriving an index. More rapidly evolving changes in the OLR field can then be reflected by projection of less filtered OLR that includes higher frequencies onto the intraseasonal spatial modes. This is still effective at reducing the influence of other convectively coupled modes, since those are generally associated with a much smaller OLR spatial scale than the intraseasonal EOFs (Kiladis et al. 2009). Although the derivation of the OMI involves calculating running EOFs of OLR, implementation is straightforward once these are obtained, and only requires the projection of filtered observed or model derived OLR or rainfall onto the daily EOF spatial patterns. Since OLR EOFs do not change much through the solstice seasons, a single pair of EOFs, such as those obtained by Kikuchi et al. (2012), can also be used to derive MJO indices for those times of the year through the projection of 20-96 day or other bandpass filtered OLR data. The FMO EOF procedure provides another index using more easily derived latitudinally averaged OLR, and projection of filtered OLR data onto the original WH04 OLR EOFs is yet another alternative.

One drawback of indices such as the OMI and FMO is that they cannot be exactly calculated for real time monitoring due to the pre-filtering necessary to apply them. However, even a filtered index such as OMI can be approximated near end points using the approach developed by Kikuchi et al. (2012), as long as the spatial EOFs derived from the fully filtered fields are used for projection. Real-time data can be easily smoothed for this, using running averages up to the endpoint, as shown in Section 5. Nevertheless, for studies where retrospective data allow for better filtering, the OMI and FMO certainly do a better job in categorizing the convective evolution of individual events, as shown in the preceding sections of this paper.

With regard to the evaluation of model output using MJO indices (e.g. Gottschalck et al. 2010), OLR-based indices are certainly a more difficult target than an index such as RMM (Hamill and Kiladis 2013; Wang et al. 2013). This is because the planetary scale circulation associated with the MJO is largely dominated by the rotational component, which imparts

a measure of persistence to the flow that general circulation models can more successfully maintain and evolve than the multi-scale convective signal tied to the vagaries of a particular convective parameterization and other model physics. Since forecast runs generally involve relatively short lead times, when OLR or rainfall is verified, similar procedures used for real time smoothing can also be applied for model output with observed OLR EOFs as the target. If sufficiently long runs are not available for adequate smoothing, however, then the OLR component of RMM can still be used (Hamill and Kiladis 2013).

We have avoided the issue of whether the large-scale circulation pattern should be considered as a *defining* aspect of the MJO, and instead focused on the goal of tracking the MJO convective signal. An evolving circulation appears to be tied to MJO convective initiation at times (e.g. Lin et al. 2009; Ray and Zhang 2010; S13; Ling et al. 2013; Zhao and Zhou 2013). For instance, during the DYNAMO field campaign the extended range forecast team predicted the onset of MJO1 convection over the Indian Ocean on the basis of the prior strong RMM signal in Fig. 6a, which was primarily due to circulation over the Western Hemisphere (G13). However these signals are not reliably present, and once established, the convective component provides the critical link to the instability mechanism of the disturbance (Raymond and Fuchs 2009; Khouider et al. 2012; Liu and Wang 2012) and its teleconnections (Seo and Song 2012; Dole et al. 2013). Another caveat is that even without a convective signal, other modes excited for example by extratropical mountain torques (Weickmann and Berry 2009) exist within the same intraseasonal frequency range as the MJO. These would still be present without tropical convective activity, and recent evidence suggests that such modes can significantly affect tropical circulation on the MJO time scale (Adames et al. 2013).

The OMI and FMO provide two more options to the wide variety of indices that have been designed to track the MJO convective signal using differing filter bands or techniques, depending on the application. For example, more elaborate methods developed by Roundy and Schreck (2009) and Roundy (2012) use many tens of extended OLR EOFs to capture

the zonally, meridionally and temporally varying structure of the MJO and convectively coupled waves. There will doubtlessly be many more ways to categorize the MJO developed in the future. Consideration of MJO metrics that rely on proxies of rainfall, and careful comparison with those that are more dynamically based will be of great utility in unraveling the complex relationship between the MJO diabatic heating field and its accompanying large-scale dynamics.

Acknowledgments.

ERA Interim reanalysis data were provided by NCAR. Comments by Kathy Pegion, Pedro Silva Dias, Harry Hendon and Joseph Biello greatly helped to improve the presentation. The OMI and FMO indices, along with their real time counterparts and the spatial EOFs, can be obtained at: <http://www.esrl.noaa.gov/psd/mjo/mjoindex/>

REFERENCES

- 588 Adames, A. F., J. Patoux, and R. C. Foster, 2013: The contribution of extratropical waves
589 to the MJO wind field. *J. Atmos. Sci.*, (*in press*).
- 590 Arguez, A., P. Yu, and J. J. O. Brien, 2008: A new method for time series filtering near
591 endpoints. *J Atmos. Ocean Tech.*, **25**, 534–546.
- 592 Belanger, J. I., J. A. Curry, and P. J. Webster, 2010: Predictability of North Atlantic tropical
593 cyclone activity on intraseasonal time scales. *Mon. Wea. Rev.*, **138**, 4362–4374.
- 594 Dee, D. P., et al., 2011: The ERA-Interim reanalysis: configuration and performance of the
595 data assimilation system. *Quart. J. Roy. Meteor. Soc.*, **137**, 553–597.
- 596 DeMott, C. A., C. Stan, and D. A. Randall, 2013: Northward propagation mechanisms of the
597 boreal summer intraseasonal oscillation in the ERA-Interim and SP-CCSM. *J. Climate*,
598 **26**, 1973–1992.
- 599 Dias, J., S. Leroux, S. N. Tulich, and G. N. Kiladis, 2013: How systematic is organized
600 tropical convection within the MJO? *Geophys. Res. Lett.*, **40**, 1420–1425.
- 601 Dole, M. H., R., et al., 2013: The making of an extreme event: Putting the pieces together.
602 *Bull. Amer. Meteor. Soc.* (*in press*).
- 603 Gloeckler, L. C. and P. E. Roundy, 2013: Modulation of the extratropical circulation by
604 combined activity of the Madden–Julian Oscillation and equatorial Rossby waves during
605 boreal winter. *Mon. Wea. Rev.*, **141**, 1347–1357.
- 606 Gottschalck, J., P. E. Roundy, C. J. Schreck, A. Vintzileos, and C. Zhang, 2013: Large-scale
607 atmospheric and oceanic conditions during the 2011-2012 dynamo field campaign. *Mon.*
608 *Wea. Rev.* (*in press*).

609 Gottschalck, J., et al., 2010: A framework for assessing operational Madden Julian oscillation
610 forecasts: A CLIVAR MJO working group project. *Bull. Amer. Meteor. Soc.*, **91**, 1247–
611 1258.

612 Hamill, T. M. and G. N. Kiladis, 2013: An all-season real-time multivariate MJO index:
613 Development of an index for monitoring and prediction. *Mon. Wea. Rev.* (*in press*).

614 Johnson, R. H. and P. E. Ciesielski, 2013: Structure and properties of Madden-Julian Oscil-
615 lations deduced from DYNAMO sounding arrays. *J. Atmos. Sci.* (*in press*).

616 Kessler, W. S., 2001: EOF representation of the Madden-Julian Oscillation and its connec-
617 tion with ENSO. *J. Climate*, **14**, 3055–3061.

618 Khouider, B., Y. Han, A. J. Majda, and S. N. Stechmann, 2012: Multiscale waves in an MJO
619 background and convective momentum transport feedback. *J. Atmos. Sci.*, **69**, 915–933.

620 Kikuchi, K. and Y. N. Takayabu, 2003: Equatorial circumnavigation of moisture signal asso-
621 ciated with the Madden-Julian Oscillation MJO during boreal winter. *J. Meteor. Japan*,
622 **44**, 25–43.

623 Kikuchi, K., B. Wang, and Y. Kajikawa, 2012: Bimodal representation of the tropical in-
624 traseasonal oscillation. *Clim. Dyn.*, **10**, 1989–2000.

625 Kiladis, G. N., M. C. Wheeler, P. T. Haertel, K. H. Straub, and P. E. Roundy, 2009:
626 Convectively coupled equatorial waves. *Rev. Geophys.*, **47**, RG2003.

627 Klotzbach, P. J., 2010: On the Madden-Julian Oscillation–atlantic hurricane relationshiop.
628 *J. Climate*, **23**, 282–293.

629 Lau, K. H. and P. H. Chan, 1988: Intraseasonal and interannual variations of tropical
630 convection: A possible link between the 40–50 day oscillation and ENSO? *J. Atmos. Sci.*,
631 **118**, 506–521.

- 632 Lau, K. H. and D. E. Waliser, 2011: *Intraseasonal variability in the atmosphere-ocean climate*
633 *system*. Praxis, New York, 646 pp.
- 634 Lee, J. Y., B. Wang, M. C. Wheeler, X. Fu, D. E. Waliser, and I., 2013: Realtime mul-
635 tivariate indices for the boreal summer intraseasonal oscillation over the asian summer
636 monsoon region. *Clim. Dyn.*, **40**, 493–509.
- 637 Liebmann, B. and C. A. Smith, 1996: Description of a complete (interpolated) outgoing
638 long-wave radiation dataset. *Bull. Amer. Meteor. Soc.*, **77**, 1275–1277.
- 639 Lin, H., G. Brunet, and J. Derome, 2009: An observed connection between the North Atlantic
640 oscillation and the Madden-Julian oscillation. *J. Climate*, **22**, 364–380.
- 641 Ling, J., C. Zhang, and P. Bechtold, 2013: Impacts of upscale heat and momentum transfer
642 by moist Kelvin waves on the Madden-Julian Oscillation: a theoretical model study. *Clim.*
643 *Dyn.*, **40**, 213–224.
- 644 Liu, F. and B. Wang, 2012: A frictional skeleton model for the Madden-Julian Oscillation.
645 *J. Atmos. Sci.*, **69**, 2749–2758.
- 646 Lorenc, A. C., 1984: The evolution of planetary-scale 200 mb divergent flow during the
647 FGGE year. *Quart. J. Roy. Met. Soc.*, **110**, 427–441.
- 648 Madden, R. A. and P. R. Julian, 1971: Detection of a 40-50-day oscillation in the zonal wind
649 in the tropical Pacific. *J. Atmos. Sci.*, **29**, 1109–1123.
- 650 Madden, R. A. and P. R. Julian, 1972: Description of global-scale circulation cells in the
651 tropics with a 40–50 day period. *J. Atmos. Sci.*, **29**, 1109–1123.
- 652 Maloney, E. D. and D. L. Hartmann, 1998: Frictional moisture convergence in a composite
653 life cycle of the Madden-Julian oscillation. *J. Climate*, **11**, 2387–2403.
- 654 Masunaga, H., 2007: Seasonality and regionality of the Madden-Julian Oscillation, Kelvin
655 wave, and equatorial Rossby wave. *J. Atmos. Sci.*, **64**, 4400–4416.

656 Matthews, A. J., 2008: Primary and successive events in the Madden-Julian Oscillation.
657 *Quart. J. Roy. Met. Soc.*, **134**, 439–453.

658 Matthews, A. J., B. J. Hoskins, and M. Masutani, 2004: The global response to tropical
659 heating in the Madden-Julian Oscillation during the northern winter. *Quart. J. Roy. Met.*
660 *Soc.*, **130**, 1991–2011.

661 Moncrieff, M., D. E. Waliser, M. J. Miller, M. A. Shapiro, G. R. Asrar, and J. Caughey,
662 2012: Multiscale organization and the YOTC virtual global field campaign. *Bull. Amer.*
663 *Meteor. Soc.*, **77**, 1171–1187.

664 Moore, R. W., O. Martius, and T. Spengler, 2010: The modulation of the subtropical and ex-
665 tratropical atmosphere in the Pacific Basin in Response to the Madden-Julian Oscillation.
666 *Mon. Wea. Rev.*, **138**, 2761–2778.

667 North, G. R., T. L. Bell, R. F. Cahalan, and F. J. Moeng, 1982: Sampling errors in the
668 estimation of empirical orthogonal functions. *Mon. Wea. Rev.*, **110**, 699–706.

669 Rashid, H. A., H. H. Hendon, M. C. Wheeler, and O. Alves, 2011: Prediction of the Madden-
670 Julian Oscillation with the POAMA dynamical prediction system. *Clim. Dyn.*, **36**, 649–661.

671 Ray, P. and C. Zhang, 2010: A case study of the mechanics of extratropical influence on the
672 initiation of the Madden-Julian Oscillation. *J. Atmos. Sci.*, **67**, 515–528.

673 Raymond, D. J. and Z. Fuchs, 2009: Moisture modes and the Madden-Julian Oscillation. *J.*
674 *Climate*, **22**, 3031–3046.

675 Roundy, P., 2012: Observed structure of convectively coupled waves as a function of equiv-
676 alent depth: Kelvin waves and the Madden-Julian Oscillation. *J. Atmos. Sci.*, **69**, 2097–
677 2106.

678 Roundy, P. E. and W. M. Frank, 2004: Applications of a multiple linear regression model to

the analysis of relationships between eastward- and westward-moving intraseasonal modes.
J. Atmos. Sci., **24**, 3041–3048.

Roundy, P. E. and C. J. Schreck, 2009: A combined wave-number–frequency and time-extended EOF approach for tracking the progress of modes of large-scale organized tropical convection. *Quart. J. Roy. Met. Soc.*, **135**, 161–173.

Roundy, P. E., C. J. Schreck, and M. A. Janiga, 2009: Contributions of convectively coupled equatorial Rossby waves and Kelvin waves to the Real-Time Multivariate MJO indices. *Mon. Wea. Rev.*, **137**, 469–478.

Seo, K. . and S. . Song, 2012: The global atmospheric circulation response to tropical diabatic heating associated with the Madden-Julian Oscillation during northern winter. *J. Atmos. Sci.*, **69**, 79–96.

Slingo, J. M., D. P. Rowell, K. R. Sperber, and F. Nortley, 1999: On the predictability of the interannual behaviour of the Madden-Julian Oscillation and its relationship with El Nino. *Quart. J. Roy. Meteor. Soc.*, **125**, 583–609.

Sperber, K. R., 2003: Propagation and the vertical structure of the Madden-Julian Oscillation. *Mon. Wea. Rev.*, **131**, 3018–3037.

Sperber, K. R. and D. E. Waliser, 2008: New approaches to understanding, simulating, and forecasting the Madden-Julian Oscillation. *Bull. Amer. Meteor. Soc.*, **89**, 1917–1920.

Straub, K. H., 2013: MJO initiation in the Realtime Multivariate MJO Index. *J. Climate*, **26**, 1130–1151.

Thompson, D. B. and P. E. Roundy, 2013: The relationship between the Madden-Julian Oscillation and U.S. violent tornado outbreaks in the spring. *Mon. Wea. Rev.*, **141**, 2087–2095.

- Ventrice, M. J., C. D. Thorncroft, and P. E. Roundy, 2011: The Madden-Julian Oscillation’s influence on african easterly waves and downstream tropical cyclogenesis. *Mon. Wea. Rev.*, **139**, 2704–2722.
- Ventrice, M. J., M. C. Wheeler, H. H. Hendon, C. J. Schreck, C. D. Thorncroft, and G. N. Kiladis, 2013: A modified multivariate Madden Julian Oscillation index using velocity potential. *Mon. Wea. Rev.*, **141**, 4197–4210.
- Waliser, D., et al., 2012: The “year” of tropical convection (May 2008–April 2010). Climate variability and weather highlights. *Bull. Amer. Meteor. Soc.*, **77**, 1189–1218.
- Waliser, D. E., R. Murtugudde, and L. E. Lucas, 2003: Indo-Pacific Ocean response to atmospheric intraseasonal variability: 1. austral summer and the Madden-Julian Oscillation. *J. Geophys. Res.*, **108**, doi:10.1029/2003JC002002.
- Wang, B., (Ed.) , 2006: *The Asian Monsoon*. Springer, 787 pp.
- Wang, W., M.-P. Hung, S. J. Weaver, A. Kumar, and X. Fu, 2013: MJO prediction in the NCEP climate forecast system version 2. *Clim. Dyn.*, 1806–9.
- Weickmann, K. M. and E. Berry, 2009: The tropical Madden-Julian Oscillation and the global wind oscillation. *Mon. Wea. Rev.*, **137**, 1601–1613.
- Wheeler, M. and G. Kiladis, 1999: Convectively-coupled equatorial waves: Analysis of clouds in the wavenumber-frequency domain. *J. Atmos. Sci.*, **56**, 374–399.
- Wheeler, M. C. and H. H. Hendon, 2004: An all-season real-time multivariate MJO index: Development of an index for monitoring and prediction. *Mon. Wea. Rev.*, **132**, 1917–1932.
- Yoneyama, K., C. Zhang, and C. N. Long, 2013: Tracking pulses of the Madden-Julian Oscillation. *Bull. Amer. Meteor. Soc.*, (*in press*).
- Zhang, C., 2005: Madden-Julian Oscillation. *Rev. Geophys.*, **43**, 1–36.

725 Zhang, C., J. Gottschalck, E. D. Maloney, M. W. Moncrieff, F. Vitart, B. W. D. E. Waliser,
726 and M. C. Wheeler, 2013: Cracking the MJO nut. *Geophys. Res. Lett*, **40**, 1–36.

727 Zhang, C. and H. H. Hendon, 1997: Propagating and standing components of the intrasea-
728 sonal oscillation in tropical convection. *J. Atmos. Sci.*, **54**, 741–752.

729 Zhao, T. L., C. and T. Zhou, 2013: Precursor signals and processes associated with MJO
730 initiation over the tropical Indian ocean. *J. Climate*, **26**, 291–307.

List of Tables

- 1 Summary of the indices used in this study, and a description of their derivation. All fields are computed using daily data. Links to these indices can be found at: <http://www.esrl.noaa.gov/psd/mjo/mjoindex/> 32
- 2 Maximum bivariate correlations between the daily PCs of the various indices. The lag of highest correlation shown as \pm days with a positive value indicating that the index in the left column leads that in the top row. 33
- 3 The percentage of primary initiation dates that match for RMM, OMI, or FMO to within ± 3 days obtained by varying the range of parameters for each individual index used to produce Fig. 9. Percentages are shown for three thresholds: 1.0, 1.1, and 1.2 (see text). 34
- 4 The percentage of primary initiation dates that match between RMM, OMI, and FMO to within ± 3 , ± 7 , and ± 14 days obtained by varying the range of parameters used to produce Fig. 9, averaged over the three thresholds of 1.0, 1.1, and 1.2 (see text) 35

TABLE 1. Summary of the indices used in this study, and a description of their derivation. All fields are computed using daily data. Links to these indices can be found at: <http://www.esrl.noaa.gov/psd/mjo/mjoindex/>

RMM	Combined EOF of normalized OLR, U850, and U200 averaged from 15°S-15°N.
OMI	Projection of 20-96 day filtered OLR, including all eastward and westward wavenumbers onto the daily spatial EOF patterns of 30-96 day eastward filtered OLR.
FMO	Univariate EOF of normalized 20-96 day filtered OLR averaged from 15°S-15°N.
VPM	Combined EOF of normalized 200 hPa Velocity Potential, U850, and U200 averaged from 15°S-15°N.
ROMI	Real time OMI derived from OLR anomaly data with the previous 40 day mean removed and a 9 day running mean applied, projected onto the daily spatial EOF patterns of 30-96 day eastward filtered OLR.
RFMO	Real time OMI derived from OLR anomaly data with the previous 40 day mean removed and a 9 day running mean applied, projected onto the spatial EOF patterns of FMO.

TABLE 2. Maximum bivariate correlations between the daily PCs of the various indices. The lag of highest correlation shown as \pm days with a positive value indicating that the index in the left column leads that in the top row.

	OMI	RMM	FMO	VPM	RMM DJF	RMM MAM	RMM JJA	RMM SON	OMI DJF	OMI MAM	OMI JJA	OMI SON
OMI		0.70 +1	0.90 0	0.69 0	0.75 +1	0.79 -1	0.63 +2	0.67 +4				
RMM	0.70 -1		0.70 -1	0.91 -1					0.75 -1	0.79 +1	0.63 -2	0.67 -4
FMO	0.90 0	0.70 +1		0.67 0	0.74 +1	0.75 +1	0.57 +2	0.69 +3	0.95 0	0.93 +1	0.83 0	0.87 -2
VPM	0.69 0	0.91 +1	0.67 0		0.92 +1	0.93 +1	0.88 0	0.91 +1	0.72 0	0.79 +1	0.66 -2	0.66 -3

TABLE 3. The percentage of primary initiation dates that match for RMM, OMI, or FMO to within ± 3 days obtained by varying the range of parameters for each individual index used to produce Fig. 9. Percentages are shown for three thresholds: 1.0, 1.1, and 1.2 (see text).

	TH=1.0	TH=1.1	TH=1.2
RMM	23%	29%	34%
OMI	55%	56%	52%
FMO	51%	51%	50%

TABLE 4. The percentage of primary initiation dates that match between RMM, OMI, and FMO to within ± 3 , ± 7 , and ± 14 days obtained by varying the range of parameters used to produce Fig. 9, averaged over the three thresholds of 1.0, 1.1, and 1.2 (see text)

window	OMI/RMM	OMI/FMO	RMM/FMO
± 3 days	7%	30%	6%
± 7 days	13%	37%	13%
± 14 days	24%	42%	20%

List of Figures

- 1 Daily eigenvalues corresponding to an EOF analysis of 30-96 day eastward OLR between 20°S-20°N derived using a 121 day sliding window (see text). 38
- 2 Spatial patterns of OLR for a) EOF1 on January 15, b) EOF2 on January 15, c) EOF1 on July 15, and d) EOF2 on July 15. Arbitrary contour interval is 1 W m^{-2} . Blue shading corresponds to negative perturbations. 39
- 3 Regressed OLR and 850 hPa streamfunction onto the daily December-February 1979-2012 PCs of a) RMM EOF1, b) RMM EOF2, c) OMI EOF2, and d) OMI -EOF1. All fields are scaled to a +2 standard deviation PC perturbation. OLR is shaded, starting at $\pm 8 \text{ W m}^{-2}$ and 18 W m^{-2} , with negative in blue. Streamfunction contour interval is $4 \times 10^5 \text{ m}^2 \text{ s}^{-1}$. 40
- 4 As in Fig. 3, but for 200 hPa streamfunction during June-August 1979-2012 for a) RMM EOF1, b) RMM EOF2, c) OMI EOF2, and d) OMI -EOF1. Streamfunction contour interval is $10 \times 10^5 \text{ m}^2 \text{ s}^{-1}$. 41
- 5 Time-longitude diagram of OLR anomalies (shading) and MJO-filtered OLR (contours) averaged between 10°S-10°N from October 1, 2011 to April 2 2012. Negative anomalies are shown in blue, at 20 W m^{-2} intervals. Contour interval is 6 W m^{-2} . 42
- 6 Phase plots for October-December 2011 of a) RMM, c) OMI, e) FMO, and January-March 2012 b) RMM, d) OMI, and f) FMO. Dates divisible by 5 are labeled, with different colored lines representing each month as annotated on the plots. 43
- 7 As in Fig. 5, except for October 1 2009- April 2 2010 44
- 8 As in 6, except for October 2009-December 2010 and January-March 2010 45

770	9	Number of primary MJO initiation events for each sector according to the	
771		criteria given in the legend at the bottom for a) RMM, b) OMI, and c) FMO.	
772		Open blue dots represent an amplitude threshold of one, red diamonds a	
773		threshold of 1.1, and black stars a threshold of 1.2, as designated by the letter	
774		"A" in the legend. Successively darker shadings represent the combinations	
775		of the required number of days of amplitude less than the threshold prior to	
776		initiation (either 7 or 9, "L" on the legend), and the number of days then	
777		exhibiting counterclockwise rotation on the phase diagram (3, 5 and 7, "C"	
778		on the legend).	46
779	10	PC time series of a) OMI (solid, PC1 in blue, PC2 in red) and ROMI (dashed)	
780		and b) FMO and RFMO during the October 2011-March 2012 DYNAMO pe-	
781		riod. Phase plots of ROMI during c) October-December 2011 and d) January-	
782		March 2012.	47

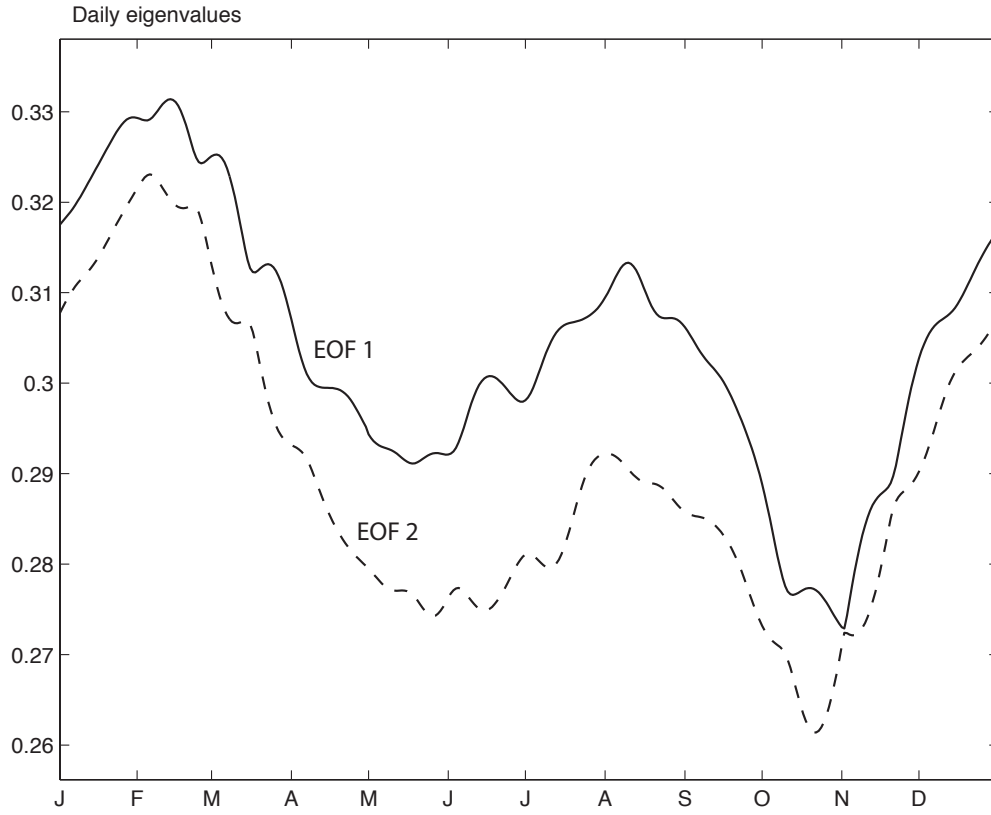


FIG. 1. Daily eigenvalues corresponding to an EOF analysis of 30-96 day eastward OLR between 20°S-20°N derived using a 121 day sliding window (see text).

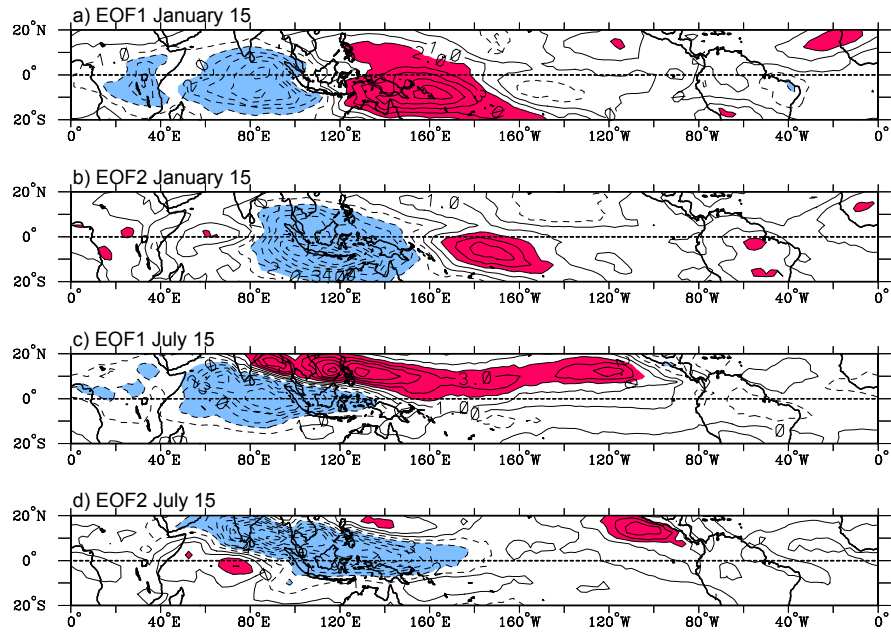


FIG. 2. Spatial patterns of OLR for a) EOF1 on January 15, b) EOF2 on January 15, c) EOF1 on July 15, and d) EOF2 on July 15. Arbitrary contour interval is 1 W m^{-2} . Blue shading corresponds to negative perturbations.

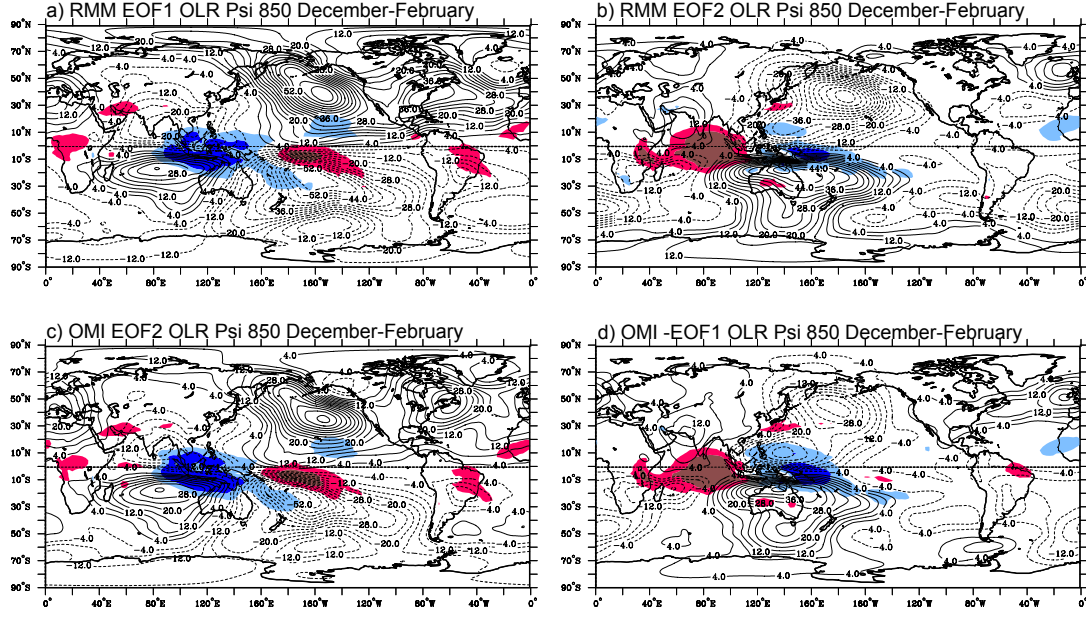


FIG. 3. Regressed OLR and 850 hPa streamfunction onto the daily December-February 1979-2012 PCs of a) RMM EOF1, b) RMM EOF2, c) OMI EOF2, and d) OMI -EOF1. All fields are scaled to a +2 standard deviation PC perturbation. OLR is shaded, starting at $\pm 8 \text{ W m}^{-2}$ and 18 W m^{-2} , with negative in blue. Streamfunction contour interval is $4 \times 10^5 \text{ m}^2 \text{ s}^{-1}$.

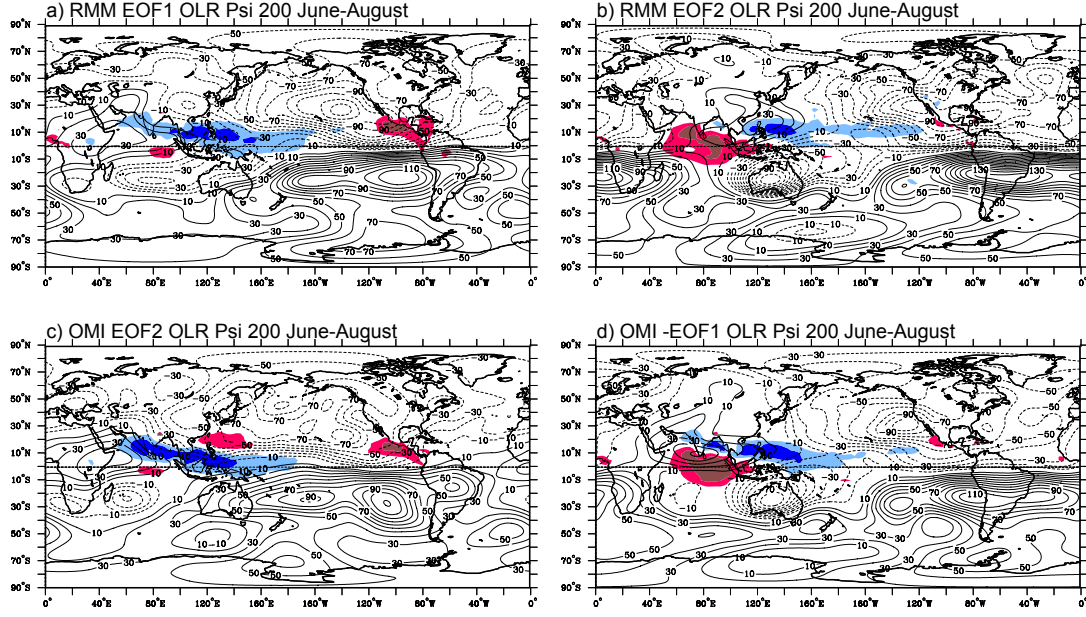


FIG. 4. As in Fig. 3, but for 200 hPa streamfunction during June-August 1979-2012 for a) RMM EOF1, b) RMM EOF2, c) OMI EOF2, and d) OMI -EOF1. Streamfunction contour interval is $10 \times 10^5 \text{ m}^2 \text{ s}^{-1}$.

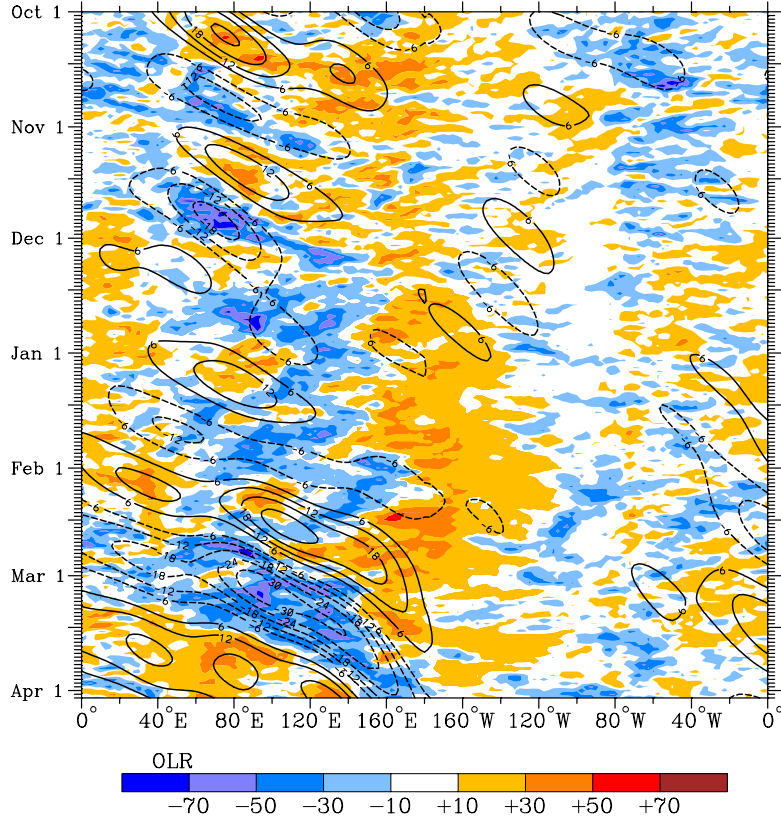


FIG. 5. Time-longitude diagram of OLR anomalies (shading) and MJO-filtered OLR (contours) averaged between 10°S - 10°N from October 1, 2011 to April 2 2012. Negative anomalies are shown in blue, at 20 W m^{-2} intervals. Contour interval is 6 W m^{-2} .

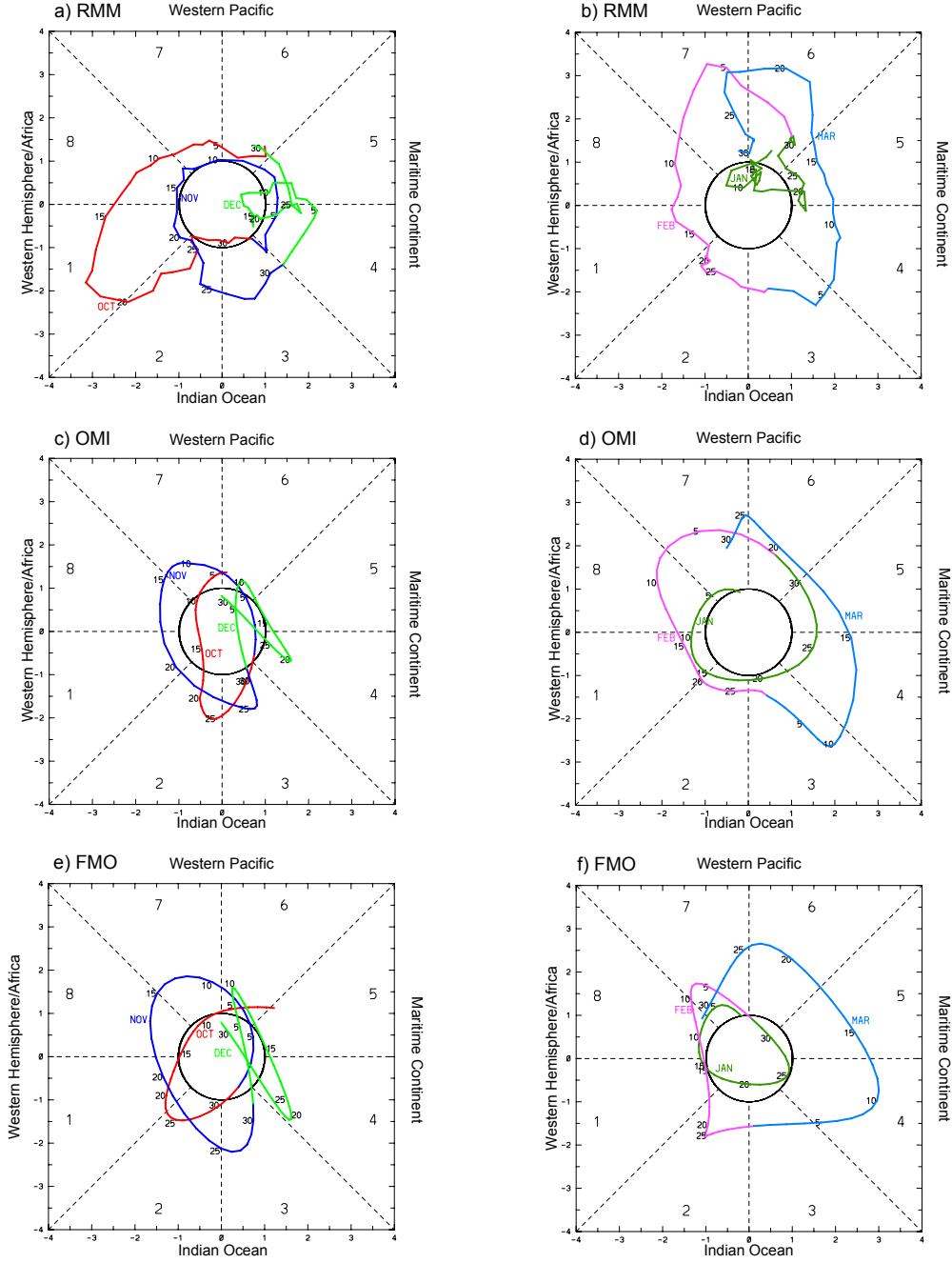


FIG. 6. Phase plots for October-December 2011 of a) RMM, c) OMI, e) FMO, and January-March 2012 b) RMM, d) OMI, and f) FMO. Dates divisible by 5 are labeled, with different colored lines representing each month as annotated on the plots.

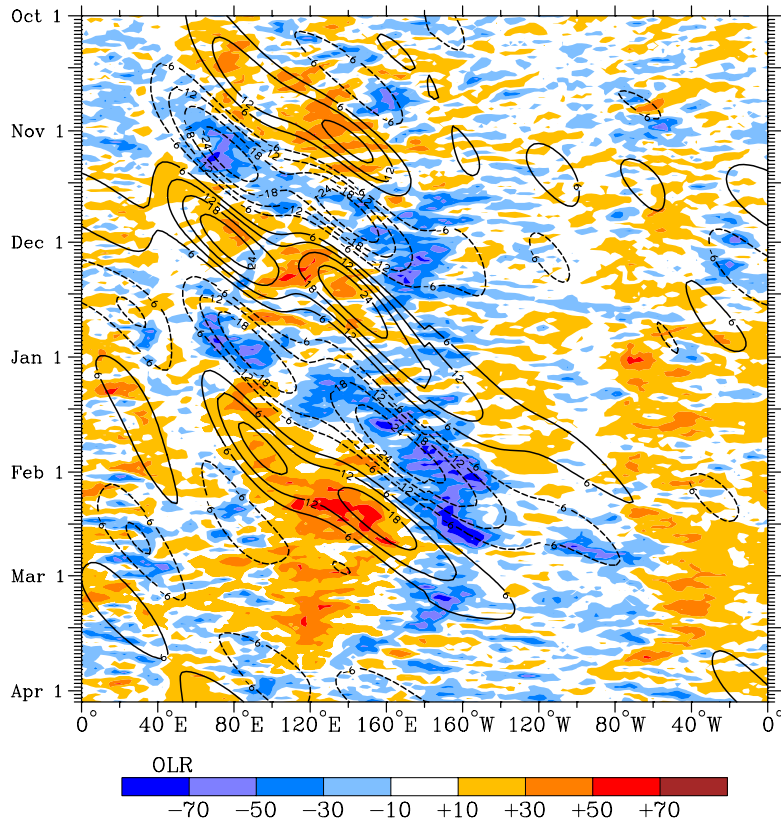


FIG. 7. As in Fig. 5, except for October 1 2009- April 2 2010

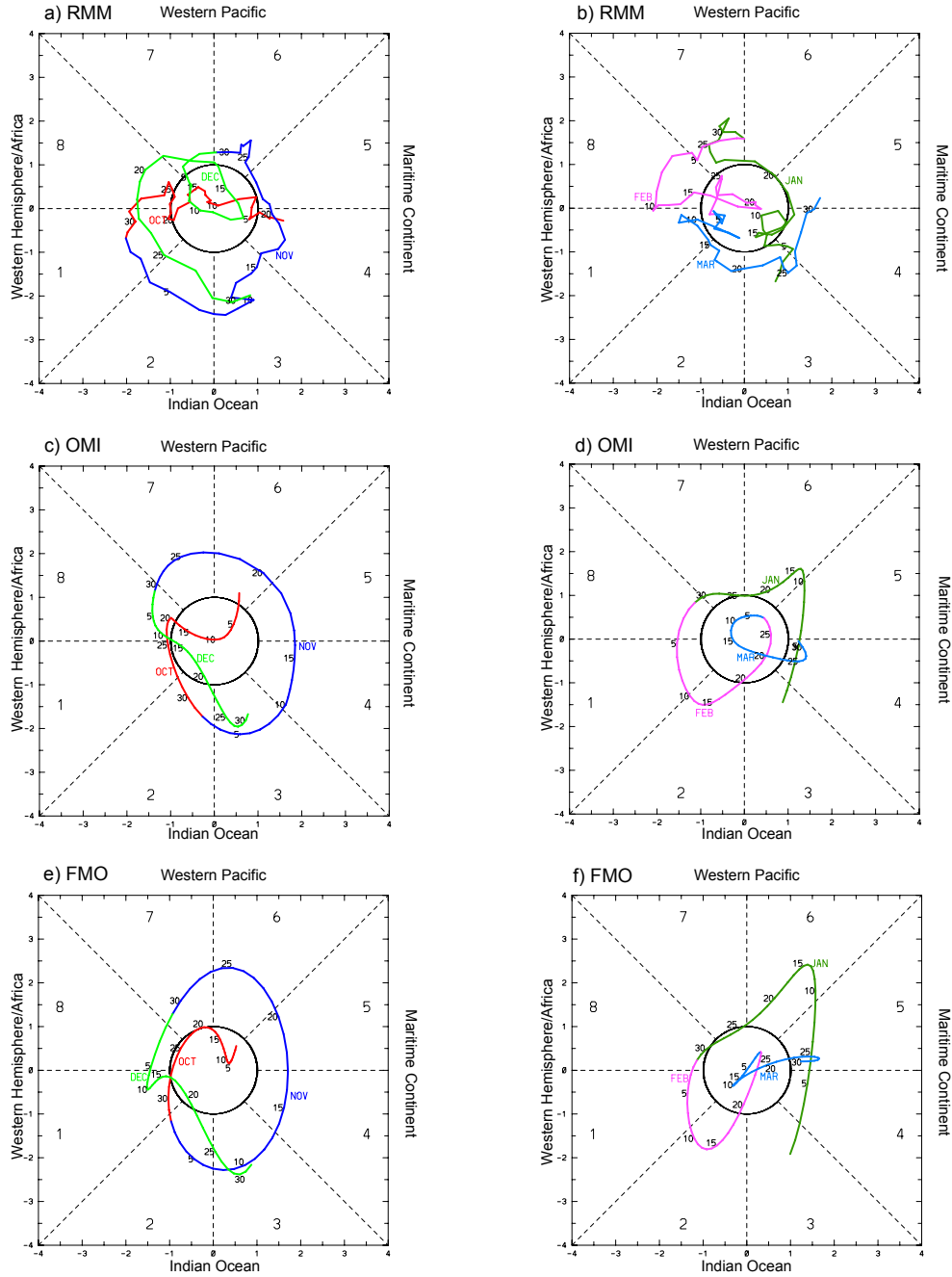


FIG. 8. As in 6, except for October 2009-December 2010 and January-March 2010

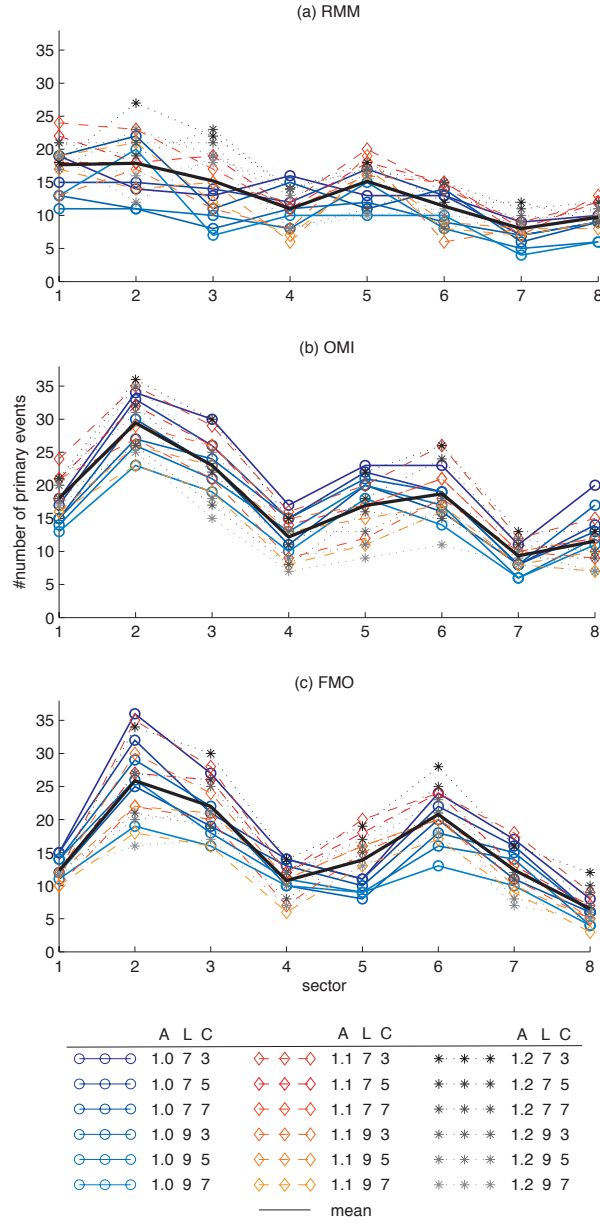


FIG. 9. Number of primary MJO initiation events for each sector according to the criteria given in the legend at the bottom for a) RMM, b) OMI, and c) FMO. Open blue dots represent an amplitude threshold of one, red diamonds a threshold of 1.1, and black stars a threshold of 1.2, as designated by the letter "A" in the legend. Successively darker shadings represent the combinations of the required number of days of amplitude less than the threshold prior to initiation (either 7 or 9, "L" on the legend), and the number of days then exhibiting counterclockwise rotation on the phase diagram (3, 5 and 7, "C" on the legend).

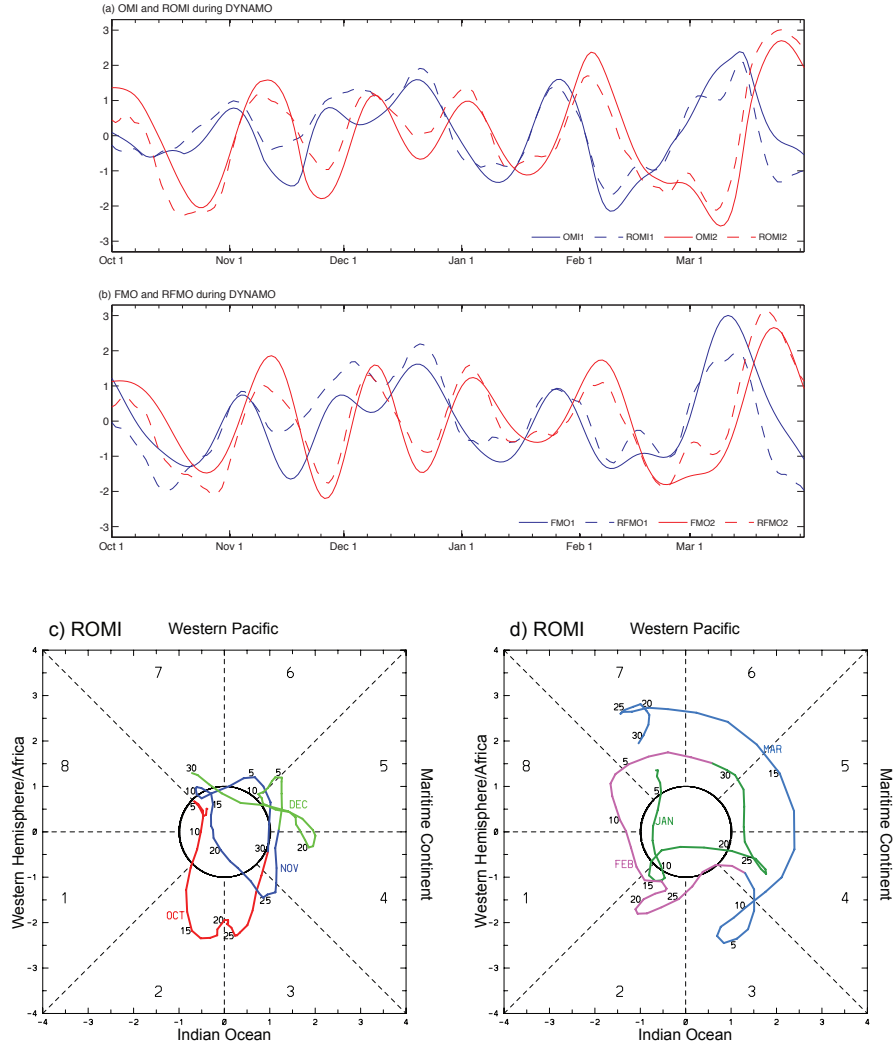


FIG. 10. PC time series of a) OMI (solid, PC1 in blue, PC2 in red) and ROMI (dashed) and b) FMO and RFMO during the October 2011-March 2012 DYNAMO period. Phase plots of ROMI during c) October-December 2011 and d) January-March 2012.